JOURNAL OF THE AMERICAN CHEMICAL SOCIETY

Article

pubs.acs.org/JACS

DFT-Chemical Pressure Analysis: Visualizing the Role of Atomic Size in Shaping the Structures of Inorganic Materials

Daniel C. Fredrickson*

Department of Chemistry, University of Wisconsin—Madison, 1101 University Avenue, Madison, Wisconsin 53706, United States

S Supporting Information

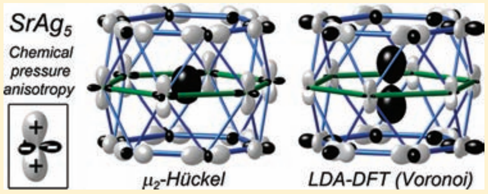

ABSTRACT: Atomic size effects have long played a role in our empirical understanding of inorganic crystal structures. At the level of electronic structure calculations, however, the contribution of atomic size remains difficult to analyze, both alone and relative to other influences. In this paper, we extend the concepts outlined in a recent communication to develop a theoretical method for revealing the impact of the space requirements of atoms: the density functional theory-chemical pressure (DFT-CP) analysis. The influence of atomic size is most pronounced when the optimization of bonding contacts is impeded by steric repulsion at other contacts, resulting in nonideal interatomic distances. Such contacts are associated with chemical pressures (CPs) acting upon the atoms involved. The DFT-CP analysis allows for the calculation and interpretation of the CP distributions within crystal structures using DFT results. The method is demonstrated using the stability of the Ca_2Ag_7 structure over the simpler $CaCu_5$-type alternative adopted by its Sr-analogue, $SrAg_5$. A hypothetical $CaCu_5$-type $CaAg_5$ phase is found to exhibit large negative pressures on each Ca atom, which are concentrated in two symmetry-related interstitial spaces on opposite sides of the Ca nucleus. In moving to the Ca_2Ag_7 structure, relief comes to each Ca atom as a defect plane is introduced into one of these two negative-pressure regions, breaking the symmetry equivalence of the two sides and yielding a more compact Ca coordination environment. These results illustrate how the DFT-CP analysis can visually and intuitively portray how atomic size interacts with electronics in determining structure, and bridge theoretical and experimental approaches toward understanding the structural chemistry of inorganic materials.

INTRODUCTION

The concept of atomic size is central to our empirical understanding of inorganic crystal structures, as is seen in the sphere-packing views of metals and intermetallic phases,[1] the radius ratio rules for simple ionic solids,[2] and the usefulness of van der Waals radii in understanding molecular packing.[3] From the point of view of electronic structure calculations, however, atomic size remains a nebulous factor. While an array of tools for the analysis of bonding interactions is available—such as the crystal orbital overlap and Hamilton populations,[4] as well as the electron localization function and indicator[5]—the influence of the space requirements of atoms is usually overlaid on these electronic structure results through empirical arguments.[6] A tighter integration of the role of atomic size into electronic structure analysis would deepen interactions between the experimental and theoretical approaches to inorganic materials.

In this paper, we develop a theoretical method for analyzing the combined impact of atomic size and electronics on interatomic interactions: the DFT-chemical pressure analysis, which builds on the concepts of energy and stress densities[7] to render quantum mechanically the empirical idea of chemical pressure.[8] The basis for this approach stems from the electronic packing frustration model in intermetallics we described in a recent communication.[9] In the dense atomic packing of metals and alloys, correlations among the interatomic distances prevent structures from optimizing individual bonding interactions independently from each other. Bond formation at certain contacts can then become stunted by steric repulsion at other contacts where there is not sufficient electronic support for shorter distances. One outcome of such frustration would be contacts with nonideal distances within the crystal structure, each of which exerts pressure on the participating atoms. Such local pressures can be interpreted with the concept of chemical pressure (CP): pressure exerted by the constraints of a chemical system, rather than by an external force.

The insights into structural chemistry obtainable from the analysis of chemical pressures were illustrated with μ_2-Hückel calculations on the Yb_2Ag_7-type structure of Ca_2Ag_7 (Figure 1).[9] Here the visualization of CP distributions revealed that the simpler structural alternative offered by the related $CaCu_5$ type places large negative pressures on the Ca, which are relieved upon adopting the superstructure. The results highlight the potential benefits of analyzing the combined influence of the electronic structure and atomic size on inorganic crystal structures as a whole.

However, the very features of the μ_2-Hückel model that facilitated the creation of the CP analysis (simplicity, transparency, and foundations in orbital interactions) also limit its generality. While we have been able to extend its use to other intermetallics, such as Ca_5Cu_2Cd and $Ca_2Cu_2Cd_9$,[10] the method requires a faithful translation of the DFT electronic

Received: January 20, 2012
Published: March 10, 2012

dx.doi.org/10.1021/ja300685j | J. Am. Chem. Soc. 2012, 134, 5991−5999

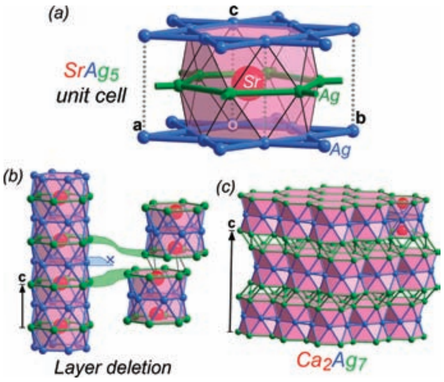

Figure 1. Beginning with (a) the $CaCu_5$-type (as observed for $SrAg_5$), (b) the deletion of kagome layers (blue) produces (c) the structure of Ca_2Ag_7.

structure into a Hückel tightbinding model. Such a translation becomes challenging for complex crystal structures with many symmetry-distinct sites, and it would be expected to fail when substantial ionicity is expected, as in oxides.

Extracting chemical pressure information directly from the output of DFT calculations would largely resolve these issues, allowing for the CP analysis of any crystal structure for which a DFT treatment is deemed sufficient. Analytical expressions have been given for the spatial variation of the quantum mechanical stress within structures,[7] but these have found few applications to chemical systems.[11,12] This may be due, in part, to difficulty in implementing the equations using the output available from commonly used computational packages. In this paper, we will build a simpler, numerical scheme in which crystal structures are divided into a finely spaced grid of voxels (the 3D analogues of pixels), whose pressures can be calculated in a straightforward manner from DFT results (using a handful of programs available on the author's homepage, as described in the Theoretical Procedures section).

In developing this method, we will again use the structure of Ca_2Ag_7 as a model system. This phase exemplifies a vast variety of intermetallics for which empirical reasoning suggests the involvement of atomic sizes. The collective experience of the literature is that $CaCu_5$-type phases are likely to form from combinations of alkaline earth or lanthanide elements with late transition metals in ratios near 1:5.[13] This is the case in the Sr−Ag system, where $SrAg_5$ occurs.[14] Upon replacing Sr with Ca, however, no such compound is encountered.[15] Instead, the closest analogue that has been structurally characterized is the Yb_2Ag_7-type Ca_2Ag_7, in which slabs of the $CaCu_5$ type are separated by defect planes (Figure 1b).[16]

Why does the substitution of Sr with Ca have such significant structural consequences? As both are alkaline earth elements, with two weakly held valence electrons, their most conspicuous difference is in their atomic sizes. Ca's atomic radius is about 10% smaller than that of Sr (1.97 Å vs 2.15 Å).[17] We might then hypothesize that the Ca_2Ag_7 structure emerges because a Ca atom is too small for the coordination environment offered by a hypothetical $CaCu_5$-type $CaAg_5$ phase. We could proceed to strengthen this argument through compiling references to the presence or absence of other $CaCu_5$-type phases in related binary systems. Instead, over the course of this paper, we will see how DFT calculations can be used to directly and vividly reveal how atomic size can work within its electronic context to direct the crystal structures of inorganic materials.

CHEMICAL PRESSURE DISTRIBUTIONS FROM DFT

An approach to extracting chemical pressure distributions from DFT results can be obtained by extending the reasoning underlying the μ_2-Hückel CP analysis. The μ_2-Hückel total energy can be expressed as a simple sum over on-site terms and pairwise orbital interaction energies, each associated with an individual atom or interatomic contact in the structure.[18] This spatial distribution of the energy allows us to similarly resolve the pressure experienced by the phase $(-\partial E/\partial V)$ into an average over pressure contributions arising from these structural features.

The elegant form of the total energy expressions of the Kohn−Sham DFT permits a similar spatial decomposition of significant contributions to the energy of the system. Specifically, the DFT total energy can be written as

$$E_{\mathrm{DFT}} = \iiint_{\mathrm{cell}} \left(-\frac{1}{2} \sum_j o_j \psi_j^* \nabla^2 \psi_j + (v_{\mathrm{local}} + v_{\mathrm{Hartree}} \right.$$
$$\left. + \varepsilon_{\mathrm{xc}})\rho(\vec{r}) \right) \mathrm{d}\tau + E_{\mathrm{nonlocal}} + E_{\mathrm{Ewald}} + E_{\alpha}$$

where o_j is the occupancy of the one electron eigenfunction ψ_j.[19] The terms within the integral correspond respectively to the kinetic energy of the valence electrons, the interaction energy of the electrons with the local components of the atomic pseudopotentials, the Coulombic self-interaction of the electron density, and the exchange-correlation energy. The last three terms in the integral are measured relative to the potential energy of the system consisting of the ion cores immersed in a homogeneous, exchange/correlation-free electron gas, whose energy is given by the final terms $E_{\mathrm{Ewald}} + E_{\alpha}$. The term E_{nonlocal} contains the interaction energy of the electrons with the nonlocal components of the pseudopotential, for which, as for the terms $E_{\mathrm{Ewald}} + E_{\alpha}$, it is difficult to trace energetic contributions back to specific points in space.

In this way, the total energy can be expressed as an integral over an energy density distributed over the unit cell plus a remainder,

$$E_{\mathrm{DFT}} = \iiint_{\mathrm{cell}} \rho_{\mathrm{energy}}(\vec{r})\, \mathrm{d}\tau + E_{\mathrm{remainder}}$$

or, as is more convenient for numerical work, with a sum over the energies of a high number of finite volume elements, or voxels, in place of the integral,

$$E_{\mathrm{DFT}} \approx \sum_{n}^{N_{\mathrm{voxels}}} \rho_{\mathrm{energy}}(\vec{r}_n) V_{\mathrm{voxel}} + E_{\mathrm{remainder}}$$
$$= \sum_{n}^{N_{\mathrm{voxels}}} E_{\mathrm{voxel},n} + E_{\mathrm{remainder}}$$

where N_{voxels} is the total number of voxels into which we divide the unit cell, and V_{voxel} is the volume per voxel.[20] This final equation expresses the DFT total energy in a form that is particularly well-suited to CP analysis. The spatial mapping of the energy can be converted to a pressure distribution by taking

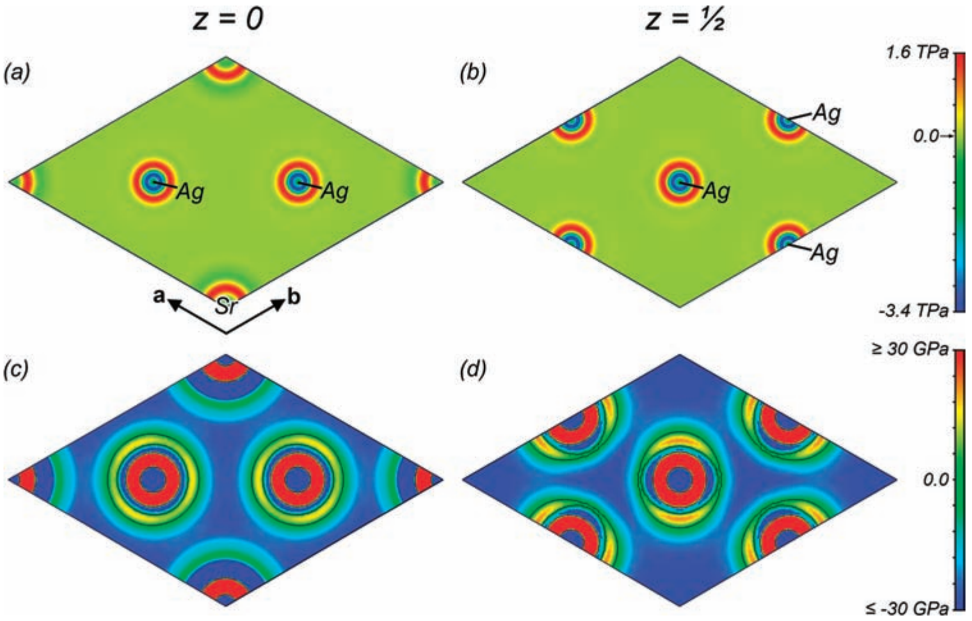

Figure 2. Cross sections of the LDA-DFT chemical pressure (CP) distribution calculated for $SrAg_5$ taken perpendicular to **c** at heights (a) $z = 0$ and (b) $z = {}^1/_2$. In parts c and d, the variations in the range −30 to 30 GPa are shown for the cross sections of parts a and b, respectively, with black contours drawn for CP = 0 to indicate transitions between negative and positive CP values.

the negative derivative of both sides of this equation with respect to unit cell volume (V_{cell}):

$$P = -\frac{\partial E_{\text{DFT}}}{\partial V_{\text{cell}}} = -\frac{1}{N_{\text{voxels}}}\frac{\partial E_{\text{DFT}}}{\partial V_{\text{voxel}}} = -\frac{1}{N_{\text{voxels}}}\sum_{n}^{N_{\text{voxels}}} P_n + P_{\text{remainder}}$$

in which the total pressure now appears as an average over a distribution of voxel pressures acting against a background remainder pressure which is treated as homogenously distributed.[21]

Let's now see what the calculation of a CP distribution in this manner can tell us about the phase $SrAg_5$ (Figure 1a). We begin by carrying out a structural optimization of the phase using LDA-DFT to obtain the equilibrium cell volume and shape.[22] Once the ground state geometry with zero overall pressure is achieved, we then perform static electronic structure calculations at three unit cell volumes: the equilibrium volume ($V_{\text{cell,O}}$), a slightly expanded volume ($V_{\text{cell,O}+\delta} = (1 + \delta)V_{\text{cell,O}}$, $\delta = 0.003$), and a slightly contracted volume ($V_{\text{cell,O}-\delta}$). Next, we use the detailed output of the calculation, together with the explicit form of the exchange-correlation functional, to calculate the voxel energies ($E_{\text{voxel},n}$'s).[23] The difference in the $E_{\text{voxel},n}$'s obtained at $V_{\text{cell,O}+\delta}$ and $V_{\text{cell,O}-\delta}$ allows us to numerically approximate the voxel pressures at $V_{\text{cell,O}}$. The $P_{\text{remainder}}$ value is then calculated either from the differences in the E_{nonlocal}, E_{Ewald}, and E_α contributions to the total energy at $V_{\text{cell,O}+\delta}$ and $V_{\text{cell,O}-\delta}$, or as the negative of the average of the voxel pressures (to set the average pressure to zero).

In Figure 2a and b, we show cross sections of the resulting CP distribution for $SrAg_5$, with color indicating the value of the pressure at each point in space. The range of pressures, from 1.6 to −3.4 TPa, is astonishing. In all cross sections, the most extreme values are concentrated around the nuclei, with the Ag atoms exhibiting spherical shells that change in color from green (ca. zero) to blue (intense negative) to red (intense positive) and back to green on moving from the nuclei outward. The Sr nuclei are decorated with a red shell of positive pressure surrounding a green center. These large pressures can be associated with the sharp response of the semicore $4s^24p^6$ and $4d^{10}$ electrons of respectively Sr and Ag to changes in the cell volume.

These corelike features appear embedded in a green background whose color corresponds to an intermediate pressure. While this background seems to be essentially flat in these images, this is only in contrast to the spherical pressure shells near the nuclei. In Figure 2c and d, we focus on the pressure range −30 to 30 GPa, a small range compared to that seen in the core region, but still corresponding to significant values in physical pressure experiments. In the plane containing the Sr atoms (Figure 2c), the CP shells now appear to ripple out further from the nuclei as their decay at longer distances is captured by the smaller pressure window. These corelike domains appear immersed in a bath of negative pressure (blue). Similar features can be seen in the kagome layer of Ag (Figure 2d), but now the first hints appear of nonspherical pressure distributions around the nuclei. The outermost shells surrounding the Ag in yellow and green are now distorted into an egg shape. This occurs against the same negative background pressure in the interstitial spaces seen in Figure 2c.

From this brief glance at the CP distribution within the $SrAg_5$ structure, we can see a significant difference compared to the cases of other tools for bonding analysis in solid state structures, such as the electron localization function and indicator (ELF and ELI). In these latter methods, bonding phenomena are often apparent in the form of peaks in the interatomic spaces. The CP distribution, however, does not appear to highlight bonding interactions in particular. Instead, it exhibits shell-like regions near atomic nuclei (with an overall positive pressure) which are balanced by a shallower negative pressure distribution occurring in the space between these core regions. The effect of interatomic interactions must then be sought in the net result of these two domains.

■ ANALYZING CP DISTRIBUTIONS WITHIN CRYSTAL STRUCTURES

Given this need to combine the roles of the core and interstitial regions in understanding the balance of pressure on the atoms of the structure, we may then expect that averaging the CP distribution over the spatial domains of individual atoms or bonds may offer a clearer view into the degree of optimization of contacts in $SrAg_5$ and other phases.

For the μ_2-Hückel CP method, this process was straightforward due to the direct mapping of CP contributors to specific pairs of orbitals. The situation is not as simple here. As the DFT-CP analysis yields a fine grid of voxel pressures rather than a list of bond pressures, one is faced with the same difficulties encountered in extracting other atomic properties from the continuous wave functions and charge densities resulting from plane wave-based DFT codes, such as atomic charge and projected density of states (DOS) curves. The determination of many atomic properties for such distributions requires a method of dividing space between the atoms of the unit cell.

Several approaches have been devised for such partitioning of space, each with their own advantages and disadvantages. One commonly used method is to draw spheres of fixed radius around each atom and include the portions of charge density or wave functions that lie within an atom's sphere in the computation of the properties of that atom (an option offered by several DFT packages). The simplicity of this approach is tempered with well-known difficulties: space cannot be filled with such a series of spheres without allowing for a high degree of overlap. One must either leave some interstitial spaces unaccounted for or count some of the same points multiple times. This problem is compounded by the lack of a definitive criterion for assigning the sphere radii. The results of this approach for CP analysis were quickly found to be too dependent on the radii choices to be considered reliable.

These issues are solved by moving away from spherical atomic volumes to a partitioning of space into Voronoi cells, in which each atom is assigned the volume of space including all points that are closer to it than any other atom.[24] The resulting cells are space-filling, so that no concerns arise regarding overlap between atomic domains or neglect of interstitial spaces. Instead, the drawbacks of using the Voronoi cells are of a chemical nature. The boundaries between neighboring cells are drawn as bisecting the line connecting the two atoms. From a chemical view, this would be reasonable for a homoatomic contact, but this could be considered coarse for a contact between two atoms of quite different sizes. In such cases, boundaries that allot more space to the larger of a pair of atoms would seem preferable. Such is offered by the atomic volumes derived from Bader's quantum theory of atoms in molecules,[25] in which boundaries between atomic domains are determined as surfaces of zero flux in the electron density.

Using these two methods based on space-filling cells, rather consistent CP results are obtained which show similarities to schemes derived from μ_2-Hückel CP analysis (Figure 3). Figure 3a shows the chemical pressures obtained for the coordination environment of the Sr in $SrAg_5$ derived from μ_2-Hückel calculations. The net CP experienced by each atom is represented by a sphere whose radius gives the magnitude of pressure. The sign of the pressure is given by the sphere color: black for negative and white for positive. This color scheme is based on an analogy to astronomy. Black spheres indicate atoms desiring the contraction of the structure, in a manner similar to how a black hole pulls its surroundings inward. White spheres indicate atoms pushing toward the expansion of the structure, much as a white hot star radiates.

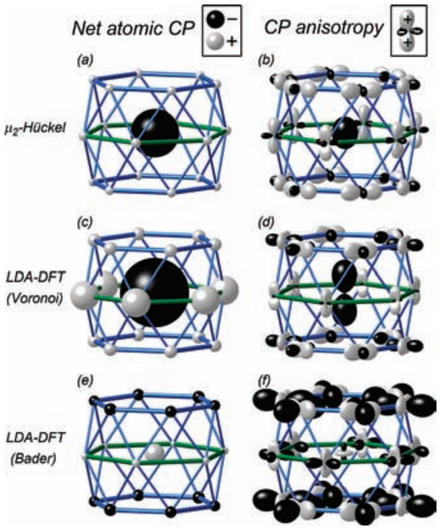

Figure 3. Integrated chemical pressure (CP) distributions for $SrAg_5$. (a) Net atomic CPs and (b) CP contributors projected onto low-order spherical harmonics ($l \leq 3$) centered on the atomic positions from a μ_2-Hückel analysis. Corresponding results for an LDA-DFT CP distribution averaged and projected within atomic Voronoi cells and Bader volumes are shown in parts c−d and e−f, respectively. The radial distance from an atom's nucleus to a point on its CP surface gives the magnitude of the pressure along that direction, with color indicating the CP sign (black, negative; white, positive). For calibration of the scales used in the plots, the Sr net CPs in parts a, c, and e are −8, −275, and 79 GPa, respectively.

The Sr atom at the center of the polyhedron appears in the μ_2-Hückel CP result as large black sphere, telling of a substantial negative pressure of −8 GPa. This indicates that the interactions between the Sr and its neighbors are underoptimized and could benefit from cell contraction. The Ag atoms, however, bear small white spheres indicative of a positive pressure. Collectively these counterbalance the negative pressure of the Sr, leading to a net pressure of zero for the phase.

The interatomic interactions underlying these net atomic CPs can be elucidated by looking at the anisotropies of the CP contributors acting on each atom. This is accomplished by projecting the pressures occurring from individual orbital interactions in the μ_2-Hückel model onto low-order spherical harmonics centered on the participating atoms and graphing the weighted sums of the functions with radial plots.

The resulting μ_2-Hückel CP anisotropy surfaces for $SrAg_5$ are shown in Figure 3b, where the same astronomical convention is used for the signs of the pressures, and the distance from an atom's nucleus to a point on its surface indicates the magnitude of the pressure along that direction. The Sr atom appears as a black ellipsoid slightly elongated vertically. Negative pressure is thus experienced by the Sr along all directions, with the contacts to the Ag atoms in the planes above and below being particularly strained. The Ag CP anisotropy surfaces reveal why these Sr−Ag contacts are prevented from contracting. White lobes point along all of the Ag−Ag contacts drawn in blue. These Ag−Ag distances are already too short, and any attempt to increase Sr−Ag bonding would exacerbate this.

How do these results compare to those obtained with the DFT-CP analysis? Parts c and e of Figure 3 show the net atomic CPs obtained from integrating the DFT-CP distributions within Voronoi cells and Bader volumes, respectively. Before describing the features present in the graphs, we first comment on the magnitudes of the pressures involved. While the net CP on the Sr in the μ_2-Hückel analysis is −8 GPa, substantially larger numbers are obtained from its DFT-CP counterparts: −275 GPa using Voronoi cells and 79 GPa using Bader volumes. When we consider how μ_2-Hückel analysis is parametrized, this is not entirely surprising. The μ_2-Hückel model was designed for an optimal fit to DFT band energies and density of states curves, and to have a net zero pressure for the phase. No constraint, however, was placed on the overall scale of the pressures involved. For this reason, it is more informative to focus on the relative CP features rather than their magnitudes.

A glance at the three sets of net CP plots in Figure 3a, c, and e reveals significant qualitative differences as well. Most striking is perhaps the placement of positive CP on the Sr when Bader volumes are used, while the other two plots agree that this site bears a high concentration of negative pressure. These differences can be largely reconciled by moving to the CP anisotropy surfaces (Figure 3b, d, and f). In all three plots, white lobes are directed along the Ag−Ag contacts drawn in blue. Each method thus highlights the overly contracted nature of the Ag sublattice. Another commonality is the presence of black lobes pointing from the Ag atoms in the upper and lower layers into the cavity occupied by the Sr. These seem to highlight underutilized bonding to the Sr atoms. From this point of view, the DFT and μ_2-Hückel CP analyses agree on the conflicting demands of Ag−Ag and Sr−Ag interactions.

Correspondences can also be perceived in the CP anisotropy of the Sr atoms. Projections of the DFT-CP distribution within Voronoi cells onto low-order spherical harmonics (Figure 3d) yield an elongated black surface on the Sr in line with that obtained from μ_2-Hückel CP analysis (Figure 3b). This time, the elongation is enhanced to the point that a deep indentation has formed around the equator. For the Bader volume result, the Sr surface is relatively small, with miniscule black lobes pointing up and down and with a white torus in the horizontal plane. All three plots (Figure 3b, d, and f) agree that the Sr experiences a stronger attraction to the Ag atoms above and below than to those in the same plane.

In comparing parts d and f of Figure 3 with each other, we see that the interstitial volumes between the Sr atom and the Ag atoms in the layers above and below are rich in negative pressure when either the Voronoi or the Bader scheme is used. However, the two methods divide the negative pressure differently between the Sr and Ag. When Voronoi cells are used, a large portion of this space is allocated to the Sr (Figure 4a), and large black lobes appear emanating from the Sr, with smaller black lobes pointing into the same region stemming from the Ag. In the Bader scheme, the boundaries between the Ag and Sr cells are drawn closer to the Sr atom (Figure 4b), in keeping with its cationic nature. With these new interatomic boundaries in place, the negative pressure lobes of the Sr have shrunk significantly while those on the Ag have expanded.

From our analysis of $SrAg_5$, several points concerning the use of DFT-CP analysis can be made. First, whereas the net atomic chemical pressure was found to be a useful quantity in the μ_2-Hückel-based approach, in this implementation the values of these pressures are highly dependent on the choice of the space-partitioning scheme. In general, allocating a large volume to one atom leads to more negative net pressure for that atom as it annexes more of the negative background pressure surrounding the ion cores. The projected CP distributions, however, are much more informative and show greater consistency both between choices for space-partitioning and with μ_2-Hückel CP results.

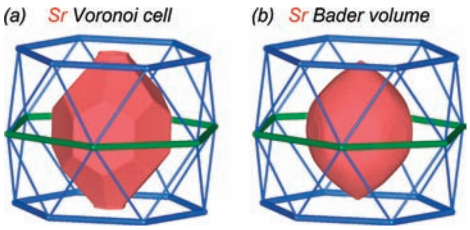

Figure 4. Atomic volumes used for the Sr atoms in $SrAg_5$ in the (a) Voronoi cell and (b) Bader volume schemes.

Another observation is that changing our method for the construction of the atomic cells leads to a change in the spatial distribution of the CP features. For $SrAg_5$, the use of Voronoi cells yields a more covalent view of the CP distribution, in which lobes of like color face each other across most contacts. The attractive and repulsive interactions between pairs of atoms then appear as mutual. The division of space into Bader volumes yields less volume to the cationic Sr atoms (Figure 4), with the negative pressures in the Sr−Ag interactions being attributed mainly to the Ag. This can be perceived as a more polar description of the CP distribution. The CP surfaces that result, with black lobes on some atoms pointing toward white lobes on other atoms, are more difficult to interpret than the corresponding features emerging from the use of Voronoi cells.

For this reason, we will employ the Voronoi cell scheme as we move on to other intermetallic systems in the following sections, while recognizing that other schemes would partition the negative pressure background differently between neighboring atoms. Further support for this choice is found in the form of the CP distribution. The features associated with specific atoms are overwhelmingly concentrated near the nuclei (Figure 2). The shallowness of the distribution in the interstitial regions means that only relatively faint variations are present with which to define boundaries between atomic cells. The most natural choice is then to make divisions at the halfway points between nuclei as in the Voronoi scheme, so that the shared regions are democratically partitioned.

■ TOWARD Ca_2Ag_7: CP ISSUES IN THE HYPOTHETICAL $CaAg_5$

So far, our emphasis has been on deriving a DFT-based version of chemical pressure analysis and illustrating its relationship to the μ_2-Hückel approach. We are now in a position to apply DFT-CP analysis to elucidating structural trends in materials. As a demonstration of such an application, we will return to the model system on which the concepts of electronic packing frustration and CP analysis were developed: the $CaCu_5$ defect structure of Ca_2Ag_7.[9] As a first step in explaining the origin of the Ca_2Ag_7, let's examine why the simpler alternative offered by the $CaCu_5$-type might desire structural modifications.

In the previous section, we investigated the chemical pressure distribution within $SrAg_5$, concluding that a conflict was occurring between the desire to shorten Sr–Ag contacts in the structure and strain within the Ag sublattice calling for an expansion of the lattice. From this scheme, we can anticipate that the replacement of Sr with Ca should deepen this tension, with Ca's smaller size leading to an increased demand for contraction of the structure against a network of already overly short Ag–Ag distances.

To test these expectations, we compare in Figure 5 the DFT-CP distribution calculated for a hypothetical $CaCu_5$-type $CaAg_5$ phase with the results we already obtained for $SrAg_5$. Figure 5 shows the atomic CP anisotropy surfaces for the two phases projected within Voronoi cells. The overall forms of the distributions are very similar. Large black lobes point from both the Ca and the Sr to the hexagons of Ag atoms above and below, and they are met by smaller black lobes protruding from the Ag. These features again emphasize the potential for stronger bonding between the Ca or Sr and the Ag atoms of these compounds. Along the Ag–Ag contacts drawn in blue, white bulbs stem from the Ag atoms in both structures, indications that these interatomic distances are too short for their electronic context.

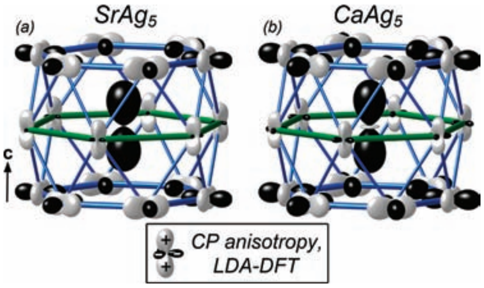

Figure 5. Comparison of integrated LDA-DFT chemical pressure (CP) distributions for $SrAg_5$ and a hypothetical $CaCu_5$-type $CaAg_5$ phase. (a and b) CP contributors within Voronoi cells projected onto low-order spherical harmonics ($l \leq 3$) for $SrAg_5$ and $CaAg_5$, respectively. The images are drawn to scale to permit the comparison of the sizes of corresponding CP features. See caption to Figure 3 for plotting conventions.

Small differences may be noted in the sizes of their corresponding features.[26] While the white lobes on the Ag are of similar sizes in both $SrAg_5$ and $CaAg_5$, their black, negative pressure ones have a greater radial extent in $CaAg_5$, indicative of greater negative pressure between the Sr/Ca–Ag contacts in the latter. Another difference is the growth of a positive pressure torus around the equator of the Ca atom. This feature suggests that, in the process of shortening the distances between the Ca and Ag atoms in the layers above and below, some positive pressure has begun to emerge in the Ca core along the shorter in-plane Ca–Ag contacts.

The DFT-CP results reveal the poor bonding environment surrounding the Ca atoms in this hypothetical $CaAg_5$ phase. The placement of the Ca atoms in the plane of the equatorial Ag atoms (green) seems to be an unstable equilibrium, with stronger Ca–Ag bonding available to Ca upon moving either above or below the plane. Such a motion, of course, would be impeded by the lengthening of the already overstretched Ca–Ag contacts on the other side. The $CaCu_5$ structure type thus does not offer any solutions to the large negative pressures on the Ca.

TRANSITION TO Ca_2Ag_7 VIEWED THROUGH DFT-CP

These DFT-CP results for $CaAg_5$ set the stage for superstructure formation. The Ca atoms appear conflicted between desires to move toward the layers of Ag atoms both above and below along *c*, with shorter contacts to one side meaning longer distances to the other. A structural transformation that breaks the equivalence between motions along +*c* and −*c* would then seem desirable. Such is provided by the Yb_2Ag_7-type structure of Ca_2Ag_7 (Figure 1b). In this structure, every other kagome layer of Ag atoms (blue) is removed from the $CaCu_5$ type (Figure 1a). Upon healing around these deletions, the remaining slabs of the $CaCu_5$ type slide relative to each other as they join together. This gives the series of the Ca polyhedra along the *c*-axis a kinked appearance. Through this process, each Ca becomes bounded on one side by a defect layer and on the other by a normal Ag kagome net (as in the $CaCu_5$ type).

In Figure 6, we follow the changes to the chemical pressures as we move from the hypothetical $CaAg_5$ phase to the observed Ca_2Ag_7 structure. Figure 6a shows a single column of Ca polyhedra from $CaAg_5$ overlaid with the CP anisotropy surfaces obtained from projection of the DFT-CP distribution within Voronoi cells. The CP surfaces of the Ca atoms resemble dz^2 orbitals with large black lobes pointing up and down along the column. The Ca atoms are ensheathed by a channel of Ag atoms whose walls are filled with white CP lobes. These features recall the tension between the drives of the Ca–Ag and Ag–Ag interactions to contract and expand the structure, respectively.

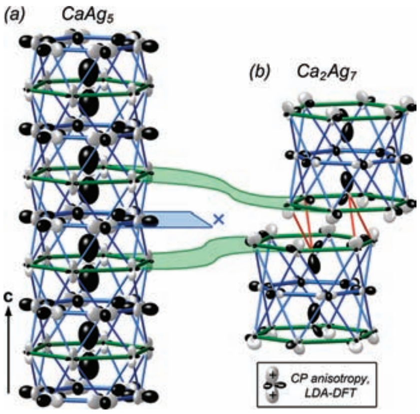

Figure 6. Structural transition between (a) a hypothetical $CaCu_5$-type $CaAg_5$ phase and (b) the Ca_2Ag_7 structure viewed with DFT-CP anisotropy surfaces. The two images follow the plotting conventions described in the caption to Figure 3 and are drawn to scale to allow for the comparison of the sizes of the CP features.

Figure 6b displays the corresponding results for Ca_2Ag_7, drawn to scale so that the lobe sizes can be compared directly to those of $CaAg_5$. As in $CaAg_5$, the Ca atoms here exhibit black lobes pointing above and below. This time, as may be expected from the new asymmetry between the top and bottom of the Ca coordination environment, these lobes are of different sizes. Those pointing toward kagome layers at the centers of the slabs are larger and resemble those of the original $CaAg_5$ phase. The other black lobe on each Ca is directed into an interface region between slabs. These features are smaller and tilted along the direction of kinking in the column. Both lobes are smaller relative to their corresponding features in $CaAg_5$. The large negative pressures on the Ca in the simpler $CaAg_5$ phase have thus been at least partially relieved in the formation of this superstructure.

A look at the Ag CP anisotropy surfaces in Ca_2Ag_7 concurs with the conclusion that this structural transformation has a soothing effect on the CP distribution. Just as in $CaAg_5$, white lobes are directed along Ag–Ag contacts, while black lobes point toward the Ca atoms. The correspondence is close toward the center of the $CaCu_5$-type slabs and weakens at the interface region, where the picture is distorted by Ag–Ag contacts between slabs. A comparison of the features in Ca_2Ag_7 with their counterparts in $CaAg_5$ shows that the majority of both the positive and negative CP interactions have been reduced in magnitude over the course of the insertion of the defect planes.

This relief of the CP features can be correlated with structural changes. In this transformation, the Ca coordination environment shrinks from including 18 Ag atoms to only 14 Ag atoms. The decrease in coordination number is a result of the sliding of the $CaCu_5$-type layers relative to each other. This mismatch places two Ag atoms of the neighboring slab at a significantly shorter distance (red in Figure 6b) than the original interlayer contacts in $CaAg_5$ (3.14 vs 3.55 Å). The combination of defect insertion and sliding between slabs thus replaces six relatively long Ca–Ag contacts with two short ones. The high degree of optimization at these new contacts is evident in the directionality of the black Ca lobes pointing into the interface. Their orientations are almost perpendicular to the nascent Ca–Ag contacts, pointing into an octahedral interstitial space defined by two Ca atoms and four Ag atoms. The soothing effect of the CP anisotropy surfaces spreads to the remainder of the structure, as the Ca now places smaller demands on its surroundings to mollify its large negative CP.

We thus arrive at a similar picture for the formation of the Ca_2Ag_7 structure to that which emerged from our earlier μ_2-Hückel CP analysis.[9] This lends the support of higher-level calculations to our earlier analogy between the adoption of this superstructure and a classic trend in physical pressure-induced phase transitions, the pressure–distance paradox.[27] In undergoing pressure induced phase transitions, structures tend to accommodate higher pressures through an increase in the coordination numbers of the atoms. As the number of bonds to each atom is increased, each individual bond is now weaker, and larger bond lengths result. This leads to a counterintuitive lengthening of bonds under increased pressures.

The transition from $CaAg_5$ to Ca_2Ag_7 can be understood by analogy to the reverse of this process: going from a high-pressure to a low-pressure phase as the physical pressure is lowered. In $CaAg_5$, the Ca atoms experience a large negative pressure. The structure responds in the formation of Ca_2Ag_7 through a decrease in the Ca coordination number by Ag from 18 to 14. As a consequence, the average Ca–Ag contact distance also decreases (3.42 vs 3.20 Å).[28] This parallel with the pressure–distance paradox strengthens our view of the Ca_2Ag_7 structure as the product of a chemical pressure-induced structural transition.

■ CONCLUSIONS

The size requirements of atoms play a central role in our thinking about molecular and solid state structures. One of the central goals of this paper has been to provide a theoretical foundation through which arguments involving atomic size can be informed using DFT calculations. Toward this end, we developed the DFT-CP analysis, in which local pressures experienced by individual volume elements in a crystal structure are calculated and assigned to atomic domains. The application of this analysis to the structures of $SrAg_5$ and Ca_2Ag_7 illustrates how the concept of chemical pressure can be used to probe the way atomic sizes act within their electronic context to influence crystal structure.

The results of the DFT-CP analysis applied to the systems examined here concur with those obtained earlier through a semiempirical μ_2-Hückel CP treatment. In $SrAg_5$, the Sr atoms exhibit overly long bonds to their Ag neighbors. The shortening of these contacts is prevented by the constraints of the Ag sublattice. Upon replacing Sr with Ca, this conflict reaches the point that a superstructure becomes necessary, with the insertion of defect planes serving to create more compact coordination environments around the Ca. The result is the Ca_2Ag_7 structure.

The correspondence between the DFT and μ_2-Hückel CP results serves not only to support our previous conclusions about the role of chemical pressure in shaping intermetallic structures but also to highlight the potential for deeper interaction between DFT and semiempirical models in guiding new synthetic experiments. While higher-level calculations are generally to be preferred when accurate numerical results are required, semiempirical methods such as μ_2-Hückel provide a much more transparent connection to experimental parameters. Through variations of the atomic parameters and the charge of the system, the dependence of the computational results on such factors as valence electron concentration and electronegativity differences can be easily explored through such models. For example, our μ_2-Hückel CP analysis of the hypothetical $CaAg_5$ indicated that the negative pressure on the Ca varies strongly with the valence electron count of the structure, with an increased electron count yielding exacerbated CPs on the Ca. This suggests the possibility of varying the impetus for defect plane insertion through elemental substitution. The validation of the μ_2-Hückel CP picture with the DFT-CP analysis strengthens these predictions. In future CP studies, we envision reversing this order: beginning with the DFT-CP analysis and then parametrizing semiempirical models to reproduce the DFT-based scheme.

While we have focused on intermetallic phases in this paper, the DFT-CP analysis is not limited to such compounds. The generality of its derivation means that it should be applicable wherever atomic size is expected to play a role against a backdrop of electronic interactions. As we apply this approach to a wider variety of systems, it will be interesting to see if CP anisotropy features continue to anticipate not only the need of structural rearrangements but also the form that these rearrangements take as in the transition from $CaAg_5$ to Ca_2Ag_7. In the hypothetical $CaCu_5$-type $CaAg_5$ phase, a need for superstructure formation was evident in two large negative pressure lobes pointing in opposite directions. These lobes are in fact symmetry-equivalent, being related by a mirror plane passing through the Ca atom. The resolution of this frustrated packing was found in breaking the equivalence of these two directions, and we can anticipate that an analogous structural adaption would be taken in other chemical systems with similar CP distributions. This raises the intriguing possibility that systems with similar CP anisotropy surfaces could give rise to similar superstructures, in a manner parallel to that of isolobal molecular systems exhibiting analogous bonding and reactivity.[29]

THEORETICAL PROCEDURES

LDA-DFT Electronic Structure Calculations. Geometrical optimizations and single-point calculations of the $CaCu_5$-type $SrAg_5$, a hypothetical $CaAg_5$ phase, and Ca_2Ag_7 (Yb_2Ag_7 type) were performed using the *ABINIT* package,[30] using the local density approximation through the exchange-correlation functional of Goedecker, Teter, and Hutter.[31] The calculations employed the Hartwigsen–Goedecker–Hutter semicore pseudopotentials provided with the package, which treat the Ag 4d and Sr 4s and 4p electrons as part of the valence set.[32] This combination of functional potentials and pseudopotentials was found to reproduce well the GGA-DFT band structures for $SrAg_5$ and $CaAg_5$ obtained in the course of our examination of these structures using the μ_2-Hückel CP analysis. The energy cutoff was set to 45 Ha for all calculations, a value which was found to converge the energy difference between the $CaCu_5$ and $AuBe_5$ structure types for both Ca–Ag and Sr–Ag to less that 1 meV per atom. Γ-centered k-point meshes distributing $9 \times 9 \times 9$ and $9 \times 9 \times 5$ points through the Brillouin zone were used for the $CaCu_5$-type and Yb_2Ag_7-type phases, respectively.

Calculation of QTAIM Atomic Volumes. Atomic volumes, defined according to the scheme of Bader's quantum theory of atoms in molecules,[25] were derived for $SrAg_5$ from the LDA-DFT valence electron density using the *Bader* program of Henkelman et al.[33] While in principle the full electron density including core electrons should be used as input for maximally quantitative results, the inclusion of the semicore Ag 4d and Sr 4s and 4p electrons proved sufficient to reproduce well the results of a similar analysis using the projector augmentor plane-wave electron density obtained during our μ_2-Hückel CP analysis of this compound. The *Bader* program also offers the capability of assigning voxels to Voronoi cells. However, in the calculations presented here, this task was performed by our program *CPintegrate*.

DFT Chemical Pressure Analysis. Programs were written for the calculation of voxel pressures as well as the averaging of the resulting voxel pressures and their projection onto spherical harmonics centered on atomic positions. The program *CPcalc_abinit* reads the electron density, total Kohn–Sham potential, Hartree potential, exchange-correlation potential, and kinetic energy density for the *ABINIT* output for three unit cell volumes, then calculates the spatial distribution of voxel pressures and adds to them a uniform background pressure to bring the average pressure to zero (which, at the equilibrium volume, corresponds to a close degree to the calculation of $P_{\text{remainder}}$). The program *CPintegrate* performs the integration and projections of the distribution within atomic spheres, Voronoi cells, or Bader volumes. The source code for both of these programs is available at the author's research group's homepage: http://www.chem.wisc.edu/~danny.

The key parameters in the use of these programs are the volume differential for the numerical calculation of the pressure and the spacing of the voxel grid. Changes in the unit cell volume of 6% and 0.6% were found to give very similar results for $SrAg_5$ and $CaAg_5$, with the latter being used for the final calculations. In terms of the grid spacings, the primitive unit cells of the $CaCu_5$- and Yb_2Ag_7-type structures were divided into $150 \times 150 \times 120$ and $120 \times 120 \times 300$ voxel grids, respectively.

Visualization of CP Distribution and Atomic Volumes. The cross sections of the $SrAg_5$ CP distribution shown in Figure 2 as well as the images of the Voronoi and Bader volumes in Figure 4 were made with the visualization program *VESTA 3* of Momma and Izumi.[34]

ASSOCIATED CONTENT

Ⓢ Supporting Information

Atomic coordinates and total energies for the optimized structures of the $CaCu_5$-type phases $SrAg_5$ and $CaCu_5$, and the Yb_2Ag_7-type phase Ca_2Ag_7. This material is available free of charge via the Internet at http://pubs.acs.org.

AUTHOR INFORMATION

Corresponding Author

*E-mail: danny@chem.wisc.edu.

Notes

The authors declare no competing financial interest.

ACKNOWLEDGMENTS

I thank Timothy Stacey and Veronica Berns for helpful discussions over the course of the development of the DFT-CP analysis, and Patrick Sims for his preliminary calculations at the early stages of this work. I also gratefully acknowledge the financial support of the University of Wisconsin—Madison, through start-up funds, and the Wisconsin Alumni Research Foundation. This research involved calculations using computer resources supported by National Science Foundation Grant CHE-0840494 and the DOE Office of Science Early Career Program (DE-SC0003947) through the Office of Basic Energy Sciences.

REFERENCES

(1) (a) Laves, F. In *Theory of alloy phases: a seminar on theory of alloy phases held during the Thirty-seventh National Metal Congress and Exposition, Philadelphia, October 15 to 21, 1955*; American Society for Metals: Cleveland, 1956; p 124. (b) Frank, F. C.; Kasper, J. S. *Acta Crystallogr.* **1958**, *11*, 184. (c) Frank, F. C.; Kasper, J. S. *Acta Crystallogr.* **1959**, *12*, 483. (d) Hume-Rothery, W.; Raynor, G. V. *The structure of metals and alloys*, 4th ed.; Institute of Metals: London, 1962. (e) Pearson, W. B. *The crystal chemistry and physics of metals and alloys*; Wiley-Interscience: New York, 1972.

(2) (a) Goldschmidt, V. M. *Trans. Faraday Soc.* **1929**, *25*, 253. (b) Pauling, L. *J. Am. Chem. Soc.* **1927**, *49*, 765.

(3) Bondi, A. *J. Phys. Chem.* **1964**, *68*, 441.

(4) (a) Hughbanks, T.; Hoffmann, R. *J. Am. Chem. Soc.* **1983**, *105*, 3528. (b) Hughbanks, T.; Hoffmann, R. *J. Am. Chem. Soc.* **1983**, *105*, 1150. (c) Dronskowski, R.; Blöchl, P. E. *J. Phys. Chem.* **1993**, *97*, 8617.

(5) (a) Becke, A. D.; Edgecombe, K. E. *J. Chem. Phys.* **1990**, *92*, 5397. (b) Savin, A.; Becke, A. D.; Flad, J.; Nesper, R.; Preuss, H.; Von Schnering, H. G. *Angew. Chem., Int. Ed.* **1991**, *30*, 409. (c) Savin, A.; Nesper, R.; Wengert, S.; Fässler, T. F. *Angew. Chem., Int. Ed. Engl.* **1997**, *36*, 1808. (d) Kohout, M.; Pernal, K.; Wagner, F. R.; Grin, Y. *Theor. Chem. Acc.* **2004**, *112*, 453. (e) Wagner, F. R.; Bezugly, V.; Kohout, M.; Grin, Y. *Chem.—Eur. J.* **2007**, *13*, 5724.

(6) (a) Amerioun, S.; Häussermann, U. *Inorg. Chem.* **2003**, *42*, 7782. (b) Mozharivskyj, Y.; Tsokol, A. O.; Miller, G. J. *Z. Kristallogr.* **2006**, *221*, 493. (c) Li, B.; Corbett, J. D. *Inorg. Chem.* **2007**, *46*, 8812. (d) Xia, S.-q.; Bobev, S. *J. Am. Chem. Soc.* **2007**, *129*, 10011. (e) Fredrickson, D. C.; Lidin, S.; Venturini, G.; Malaman, B.; Christensen, J. *J. Am. Chem. Soc.* **2008**, *130*, 8195.

(7) (a) Nielsen, O. H.; Martin, R. M. *Phys. Rev. B* **1985**, *32*, 3780. (b) Ziesche, P.; Gräfenstein, J.; Nielsen, O. H. *Phys. Rev. B* **1988**, *37*, 8167. (c) Godfrey, M. J. *Phys. Rev. B* **1988**, *37*, 10176. (d) Filippetti, A.; Fiorentini, V. *Phys. Rev. B* **2000**, *61*, 8433. (e) Rogers, C. L.; Rappe, A. M. *Phys. Rev. B* **2002**, *65*, 224117/1.

(8) For examples of the chemical pressure concept being evoked in understanding structural phenomena, see: (a) Kim, S.-J.; Ponou, S.;

Fässler, T. F. *Inorg. Chem.* **2008**, *47*, 3594. (b) DiMasi, E.; Aronson, M. C.; Mansfield, J. F.; Foran, B.; Lee, S. *Phys. Rev. B* **1995**, *52*, 14516.

(9) Fredrickson, D. C. *J. Am. Chem. Soc.* **2011**, *133*, 10070.

(10) Harris, N. A.; Hadler, A. B.; Fredrickson, D. C. *Z. Anorg. Allg. Chem.* **2011**, *637*, 1961.

(11) The application of the stress density to understanding the relative stabilities of high-pressure forms of H_2 in ref 7e is similar in spirit to the chemical pressure analysis described in this paper.

(12) Ramer, N. J.; Mele, E. J.; Rappe, A. M. *Ferroelectrics* **1998**, *206–207*, 31.

(13) Villars, P.; Calvert, L. D. *Pearson's handbook of crystallographic data for intermetallic phases*, 2nd ed.; ASM International: Materials Park, OH, 1991.

(14) Heumann, T.; Harmsen, N. Z. *Metallk* **1970**, *61*, 906.

(15) Baren, M. R. In *Binary Alloy Phase Diagrams*; Massalski, T. B., Okamoto, H., Subramanian, P. R., Kacprzak, L., Eds.; ASM International: Materials Park, OH, 1990; p 20.

(16) (a) Cordier, G.; Henseleit, R. *Z. Kristallogr.* **1991**, *194*, 146. (b) Snyder, G. J.; Simon, A. *J. Alloys Compd.* **1995**, *223*, 65.

(17) Greenwood, N. N.; Earnshaw, A. *Chemistry of the elements*, 2nd ed.; Butterworth-Heinemann: Oxford, Boston, 1997.

(18) Lee, S. *Annu. Rev. Phys. Chem.* **1996**, *47*, 397.

(19) Martin, R. M. *Electronic structure: basic theory and practical methods*; Cambridge University Press: Cambridge, U.K., New York, 2008.

(20) The voxels are of a constant size determined by the spacings of the fast-Fourier transform grid upon which ABINIT computes the real space electron density.

(21) The pressure contributions from E_{nonlocal} and E_{α} (which corrects for the use of simple Coulomb potentials in the calculation of E_{Ewald} rather than the local portions of the pseudopotentials) could in principle be divided into contributions for individual atoms. We will instead take the simpler approach of minimizing the importance of these terms by including semicore electrons as part of our valence set.

(22) The DFT-CP scheme presented here requires that the explicit form of the exchange-correlation functional be incorporated into the programs. The initial version of the code used for this paper supports just the default LDA functional used by ABINIT. In latter versions, we envision including more complex functionals that incorporate, say, the generalized gradient approximation.

(23) ABINIT offers options for the output of the kinetic energy density (ρ_{kinetic}), in addition to the total Kohn–Sham potential (v_{KS}) along with its Hartree (v_{Hartree}) and exchange-correlation (v_{xc}) components separately. From this output, the contributions to the voxel energies ($E_{\mathrm{voxel},n}$'s) can be computed through simple arithmetic. When we write $E_{\mathrm{voxel},n} = E_{\mathrm{kinetic},n} + E_{\mathrm{local},n} + E_{\mathrm{Hartree},n} + E_{\mathrm{xc},n}$, the separate terms can be calcuated as follows: $E_{\mathrm{kinetic},n} = \rho_{\mathrm{kinetic},n} V_{\mathrm{voxel}}$, $E_{\mathrm{local},n} = (v_{\mathrm{KS}} - v_{\mathrm{Hartree}} - v_{\mathrm{xc}})\rho_n V_{\mathrm{voxel}}$, and $E_{\mathrm{Hartee},n} = {}^1/_2 v_{\mathrm{Hartree}}\, \rho_n V_{\mathrm{voxel}}$, where ρ_n is the electron density at voxel n and V_{voxel} is the voxel volume. $E_{\mathrm{xc},n}$ is determined from the form of the exchange-correlation functional as $\varepsilon_{\mathrm{xc}}(\rho_n)V_{\mathrm{voxel}}$.

(24) Okabe, A.; Boots, B.; Sugihara, K.; Chiu, S. N. *Spatial tessellations: concepts and applications of Voronoi diagrams*, 2nd ed.; Wiley: Chichester, New York, 2000.

(25) Bader, R. F. W. *Atoms in molecules: a quantum theory*; Oxford University Press: Oxford, England, 1994.

(26) That the CP results for $SrAg_5$ and $CaAg_5$ are so similar might suggest that $SrAg_5$ should also experience a driving force toward superstructure formation. This could be the origin of the $SrAg_4$ compound with unknown structure in the Sr-Ag phase diagram, as given in: Baren, M. R. In *Binary Alloy Phase Diagrams*; Massalski, T. B., Okamoto, H., Subramanian, P. R., Kacprzak, L., Eds.; ASM International: Materials Park, OH, 1990; p 97.

(27) (a) Kleber, W. *Krist. Tech.* **1967**, *2*, 13. (b) Müller, U. *Inorganic structural chemistry*, 2nd ed.; Wiley: Chichester, England; Hoboken, NJ, 2007.

(28) Contraction in the closest Ca–Ca contacts also occurs, from two contacts at 4.55 Å in $CaAg_5$ to one contact at 3.69 and another at 3.72 in Ca_2Ag_7. Regardless of whether these neighbors are considered as part of the Ca coordination environment, the transition represents a decrease in the coordination number, with a shrinkage of the interatomic distances.

(29) Hoffmann, R. *Angew. Chem., Int. Ed.* **1982**, *21*, 711.

(30) (a) Gonze, X.; Rignanese, G.-M.; Verstraete, M.; Beuken, J.-M.; Pouillon, Y.; Caracas, R.; Jollet, F.; Torrent, M.; Zerah, G.; Mikami, M.; Ghosez, P.; Veithen, M.; Raty, J.-Y.; Olevano, V.; Bruneval, F.; Reining, L.; Godby, R.; Onida, G.; Hamann, D. R.; Allan, D. C. *Z. Kristallogr.* **2005**, *220*, 558. (b) Gonze, X.; Amadon, B.; Anglade, P. M.; Beuken, J. M.; Bottin, F.; Boulanger, P.; Bruneval, F.; Caliste, D.; Caracas, R.; Côté, M.; Deutsch, T.; Genovese, L.; Ghosez, P.; Giantomassi, M.; Goedecker, S.; Hamann, D. R.; Hermet, P.; Jollet, F.; Jomard, G.; Leroux, S.; Mancini, M.; Mazevet, S.; Oliveira, M. J. T.; Onida, G.; Pouillon, Y.; Rangel, T.; Rignanese, G. M.; Sangalli, D.; Shaltaf, R.; Torrent, M.; Verstraete, M. J.; Zerah, G.; Zwanziger, J. W. *Comput. Phys. Commun.* **2009**, *180*, 2582.

(31) Goedecker, S.; Teter, M.; Hutter, J. *Phys. Rev. B* **1996**, *54*, 1703.

(32) Hartwigsen, C.; Goedecker, S.; Hutter, J. *Phys. Rev. B* **1998**, *58*, 3641.

(33) (a) Henkelman, G.; Arnaldsson, A.; Jónsson, H. *Comput. Mater. Sci.* **2006**, *36*, 254. (b) Sanville, E.; Kenny, S. D.; Smith, R.; Henkelman, G. *J. Comput. Chem.* **2007**, *28*, 899. (c) Tang, W.; Sanville, E.; Henkelman, G. *J. Phys.: Condens. Matter* **2009**, *21*, 084204/1.

(34) Momma, K.; Izumi, F. *J. Appl. Crystallogr.* **2011**, *44*, 1272.